Soft Matter

PAPER

View Article Online
View Journal | View Issue

Cite this: *Soft Matter*, 2025, **21**, 9070

Inelastic effects in tube inflation: non-axisymmetric bulge instability and propagation in polyethylene tubes

Fatemeh Rouhani,[a] Abinava Ganesh Sankara Raman,[b] Jack Wurster Pazin[a] and Sachin S. Velankar *[ab]

When an elastic tube such as a rubber hose is inflated, it may sometimes show a bulge instability wherein a portion of the tube inflates much more than the rest. We show that low density polyethylene tubes show an entirely different bulge instability: first an axisymmetric bulge grows gradually, followed by rapid non-axisymmetric bulge growth into a hemispherical "bubble" prior to rupture. The pressure reaches a maximum just before the axisymmetric bulge starts growing and then decreases steeply but continuously once the bulge grows non-axisymmetrically. These behaviors are distinct from rubber tubes in which bulges are always axisymmetric, and the pressure reduces discontinuously when the bulge initiates. An approximate thin-shell model is constructed to explain bulge initiation in terms of the two chief phenomena at play: geometric effects (inflation increases the tube diameter and reduces the wall thickness), and constitutive behavior (tube wall yields at some pressure). The growth of the hemispherical bubble is attributed to the strong strain hardening of polyethylene at high strain. Finally, we show that limiting the growth of the non-axisymmetric bulge using an external constraint forces it to propagate axially—the first reported example of a non-axisymmetric propagation instability in tube inflation.

Received 29th July 2025,
Accepted 22nd October 2025

DOI: 10.1039/d5sm00778j

rsc.li/soft-matter-journal

1. Introduction

Pressurized tubes made of polymeric materials are encountered in a wide variety of situations. At sufficiently high pressure, the tubes may deform to a large extent. In applications such as pipes, arteries, or rubber tires, large deformations are undesirable and lead to failure. In situations such as soft robotic actuators, large deformations are essential to the desired function. This article is concerned with the large-deformation inflation of polymer tubes of circular cross section. Our specific focus is on the bulge instability wherein a portion of the tube inflates to a much larger extent than the rest.

The behavior of long rubber tubes or hoses is relatively well-understood.[1–4] Three behaviors are possible depending on the material properties and the ratio of the inner to outer radius. One possibility is that the tube inflates homogeneously, remaining cylindrical as it is inflated. The second is that at some stage during inflation, a bulge appears and expands locally until the tube ruptures. The third possibility is that a bulge appears but stops growing after it reaches some limiting diameter and starts propagating axially as inflation is continued (leftmost image of Fig. 1(a)[5]). This last situation is also encountered when inflating long toy balloons of the type used to make balloon animals. When the volume of the tube is increased steadily, the pressure first rises, then reduces discontinuously as the bulge initiates, followed by a plateau as the bulge propagates axially in a stable manner (yellow curve in Fig. 1(b)). These three behaviors: homogeneous inflation, bulge initiation, bulge propagation, and their pressure–volume characteristics, can all be captured by models that assume that the tubes are hyperelastic.[1,2,6–11]

As compared to the extensive literature on elastic tubes and shells, the large-deformation inflation behavior of tubes with non-elastic constitutive behaviors is sparse. Such non-elastic behaviors include viscoelasticity,[5,12,13] rate-dependence of material behavior,[5,13,14] or strain-induced changes in mechanical behavior.[14] In a previous paper on non-elastic effects,[5] we showed that the inflation of tubes made of polyurethane elastomer is distinctly different from that described above for rubber tubes. Polyurethane tubes were found to inflate with multiple axisymmetric bulges (middle image of Fig. 1(a)), and the pressure–volume behavior showed a maximum followed by a gradual, rather than abrupt, unloading (green curve in Fig. 1(b)). The tube shape was found to become more homogeneous at high inflation rates, but the pressure–volume curve was hardly affected suggesting that the pressure maximum is

[a] *Department of Mechanical Engineering and Material Science, University of Pittsburgh, Pittsburgh, PA 15261, USA. E-mail: velankar@pitt.edu*
[b] *Department of Chemical Engineering, University of Pittsburgh, Pittsburgh, PA 15261, USA*

not due to bulge initiation, but due to constitutive behavior of the material. Numerical simulations were conducted using the constitutive behavior of a viscoelastic solid whose modulus reduced exponentially with time from an initial high value to a final lower value. Despite the relative simplicity of the viscoelastic model, the simulations could reproduce most of the observations qualitatively.[5]

In this second paper on non-elastic effects in tube inflation, we turn to polyethylene tubes whose behavior strongly differs from both the rubber hoses as well as the polyurethane tubes. The rightmost image in Fig. 1(a) shows that during inflation, the tube develops a bulge that – unlike the rubber hose or the polyurethane tube – is not axisymmetric. The pressure–volume curve (red data in Fig. 1(b)) shows a maximum, followed by an initially-gradual decrease in pressure, followed by a steeper, but continuous, decrease in pressure. Unlike the other two tubes, the pressure does not approach a plateau. Instead, the bulge first grows to a nearly-hemispherical shape and eventually the tube bursts, with a fracture propagating along the circumferential direction (Fig. 1(c)). To our knowledge, there are no publications quantifying such behavior or even reporting it qualitatively.

The extensive experimental, theoretical, and computational research[1,2,15,16] on the bulging behavior of elastic tubes all deals with axisymmetric bulges. Indeed, some of the early theoretical literature[17,18] in this area argued that prismatic bulging (*i.e.* a non-axisymmetric cross-section with no axial variation) is not possible for the constitutive behavior typical for rubbery materials. Lindgreen *et al.* showed computationally that inflating a cylinder with the elastic-viscoplastic constitutive behavior of a polymer may lead to non-axisymmetric instabilities.[19,20] Merodio[21,22] showed that tubes with a non-uniform residual stress develop non-axisymmetric bulges, even if the material is elastic. If the ends of the tube are constrained, inflation can induce compressive stress, inducing the tubes to buckle in a non-axisymmetric fashion.[8,23] There are multiple computational and analytical studies on non-axisymmetric deformation of cylindrical and spherical structures under internal pressure.[24–30] Experimental studies, however, are sparse. Non-axisymmetric bulging of polymeric tubes has been noted during burst testing of plastic pipes, typically made of high-density polyethylene or polyvinyl chloride.[26,31–35] The pressurized pipe may develop a non-axisymmetric bulge that is elongated along the axial direction before bursting, and Fig. S1a–d reproduces some examples from past literature.[26,36–39] We are unaware of any experimental quantification of such bulge formation prior to burst. There do not appear to be published examples where a non-axisymmetric bulge proceeds to an almost hemispherical shape prior to failure as seen in the red tube in Fig. 1(a).

Incidentally inflation behavior of metal tubes beyond their elastic limit has been studied for many decades.[23,40–47] Metal tubes generally burst at relatively small degrees of inflation, with the rupture occurring due to the appearance of an axially-oriented crack – this is readily apparent when pipes burst due to freezing in cold weather. But bursting can sometimes be preceded by non-axisymmetric deformation[36,44] which eventually leads to a crack, see right image in Fig. S1e.[36] In fact, plastic deformation prior to failure can also be exploited, *e.g.* in the process of auto-frettage, to increase the burst pressure.[48,49]

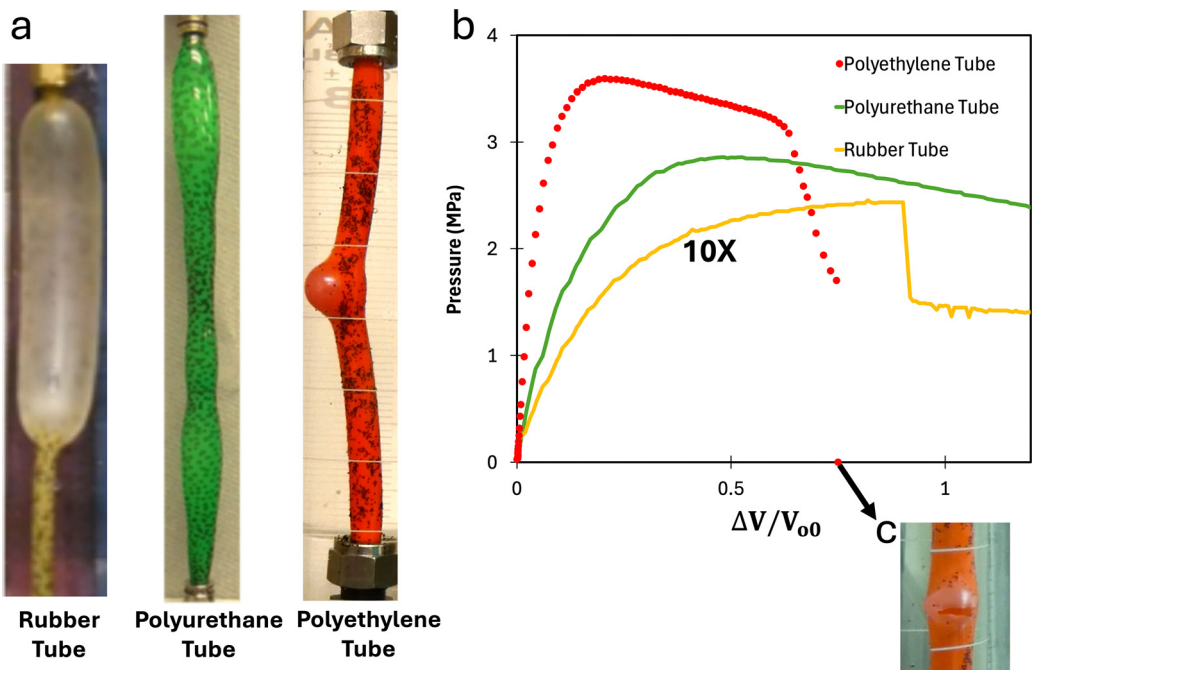

Fig. 1 (a) Behavior of various polymer tubes while being inflated at constant flow rate. All three tubes have an outer diameter of 6.35 mm. The inner diameters are 3.175 mm for the rubber tube (left), 3.97 mm for the polyurethane tube (middle), and 4.37 mm for the polyethylene tube (right). (b) Pressure *vs.* non-dimensional volume for each of the tubes from a. Here ΔV is the increase in volume due to inflation, and V_{o0} is the uninflated volume calculated based on the outer radius. The green curve and yellow curve are taken from Fig. 8 in Rouhani *et al.*[5] The pressure of the rubber tube has been multiplied by 10 for clarity. (c) Image of the red tube after burst with a circumferentially-oriented crack.

Yet, all these phenomena appear at relatively low degrees of inflation (or equivalently low circumferential strain), far smaller than the strains in this paper. In contrast, biological tissues can readily undergo large deformations without failure. Such large deformations can be accompanied by gradual failure or remodeling and growth of the tissues. In a formal sense, these changes are also non-elastic in nature and various approaches have been proposed to model such changes.[50–54]

This paper is a comprehensive experimental study of the non-axisymmetric bulge localization of the polyethylene tube shown in Fig. 1. At the outset of this research, it was not clear whether the bulge initiates at the pressure maximum or earlier/later, whether non-axisymmetry appears at initiation or later, whether viscoelasticity of the material plays a role, and at what stage the deformation becomes irreversible. The experiments in this paper were designed to address these issues. Section 2 explains the materials, equipment, and experimental methods. Section 3 first describes material properties of the tube wall and then quantifies the inflation behavior. Section 4 discusses the inflation behavior relying on a simple thin-shell model to guide the discussion. An additional experiment on non-axisymmetric bulge propagation is documented in Section 5. Section 6 concludes the paper with a brief summary.

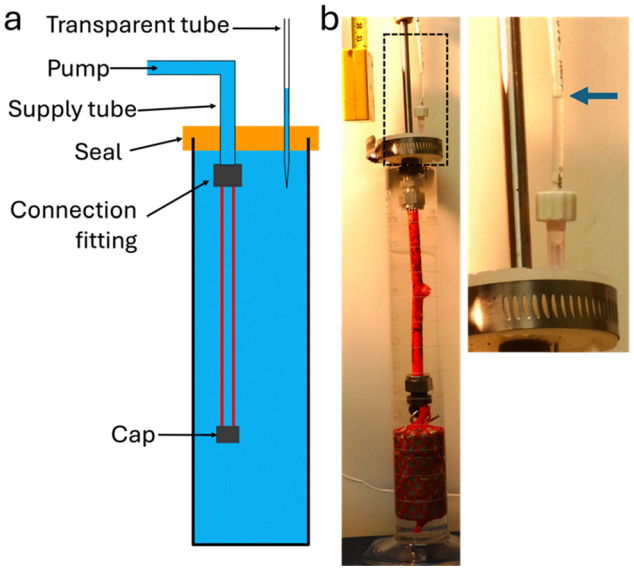

Fig. 2 Experimental setup. (a) Schematic (not-to-scale), and (b) photo of experiment where the tube has a bulge that has already burst. Black dots on the surface of the tube are marker particles. Right image is a zoomed view of the dashed rectangle where the blue arrow indicates the meniscus in the transparent "riser" tube.

2. Experimental methods

Low density polyethylene (LDPE) tubes, with an outer diameter of 1/4 inch (6.35 mm) and an inner diameter of 11/64 inch (4.37 mm), were purchased from McMaster-Carr Supply Co. Thus, the tube dimensions are R_{o0} = 3.175 mm; R_{i0} = 2.185 mm; and wall thickness h_0 = 0.99 mm. Note that the subscript o and i refer to outer and inner dimensions, and the subscript 0 refers to the undeformed state. All tubes were cut to a length of 160 mm, and accounting for the length at each end that is inserted into the fittings, the section of the undeformed tube that could inflate freely was 130 mm long, corresponding to an undeformed aspect ratio L/R_{o0} of 41, and an initial outer volume, V_{o0}, of 4.11 mL.

Tubes were inflated using a constant-flow rate piston pump (Isco Reaxys LS), and the pressure during inflation was recorded. The experiment was video-recorded with a digital camera. Prior to the experiment, the tubes were smeared with a thin layer of oil and flakes of black "glitter" were stuck on the tube. These served as markers for motion-tracking to quantify deformations.

One limitation is that the pump has an internal damper to smooth the piston displacement. At early stages of inflation when the pressure rises rapidly, the compliance of this damper, as well as the compressibility of any small bubbles trapped in the lines, may cause discrepancies between the volume displaced by the pump *vs.* the volume that is actually pumped into the tube. Therefore, instead of relying on the volume displaced by the pump, we used a "dilatometer" apparatus to measure the volume actually pumped into the polyethylene tube. The apparatus (Fig. 2) comprises a water-filled glass cylinder with a tight rubber seal with a center hole. A steel tubing, which fits the hole tightly, connects to the pump on the upper end and the polyethylene tube specimen on the lower end. The rubber seal is pierced with a needle, to which is connected a transparent plastic "riser tube" of inner diameter 2.36 mm. As the pump inflates the polyethylene tube, the water rises into the transparent tubing (inset to Fig. 2(b)) and the meniscus height can be followed by video. The height change multiplied by the known cross section of the riser tube then gives the actual volume change of the polyethylene tube, denoted ΔV.

The polyethylene tubes are supplied in a spool, and they have an intrinsic curvature. Inflation experiments were conducted with ink marks on the inner and outer curvature to test whether the intrinsic curvature affected the location of bulge initiation. We found that in most cases, bulges initiated on the "sides" *i.e.* neither on the inner nor outer curvature. To prevent this natural curvature from interfering with the quantification of the videos, a small deadload of 1.5 N was suspended from the bottom of the tube, to approximately straighten the tube. Accordingly, the axial strain can be followed readily. This axial deadload is sufficiently small that it does not affect the inflation behavior as compared to tubes without a deadload. Incidentally, from the tube modulus measured in Section S2, we estimate that this deadload induces a strain of only 0.05%.

Uniaxial tests were conducted using an Instron™ 5565 screw-driven mechanical testing machine equipped with a 50 lb (225 N) model 31 Sensotec™ transducer load cell. Details of these tests are given in Section S2.

3. Results

3.1. Mechanical properties

Mechanical properties of the tubes were measured by tensile testing, combined with quantitative video analysis to obtain

true stress *vs.* true strain relationships. Details are given in the Section S2; here we only summarize the main points. First, when tested along the axial direction, the engineering stress *vs.* engineering strain (Fig. 3(a), orange points) shows a monotonic increase. Plotting the true stress *vs.* true strain (Fig. 3(b)) gives a small-strain modulus of 160 MPa. Significant deviations from linearity appear at a stress of roughly 6.5 MPa, above which the slope of the stress–strain curve decreases significantly. Therefore, in most of the Discussion (Section 4), we adopt 6.5 MPa as the yield stress, and hence the yield strain is 0.041. A somewhat different value may be chosen for the yield stress, but it does not affect the Discussion significantly. Beyond this stress, the tubes show significant irreversible deformation. Such behaviors are typical for polyethylene. At large strain, the slope of the stress–strain curve in Fig. 3(b) increases again indicating strain hardening behavior. Second, circumferential direction tensile tests were also conducted (Fig. S2c), although as described in the Section S2, these experiments did not start from the stress-free state. In these experiments, the engineering stress *vs.* engineering strain curves (Fig. 3(a), blue points) showed a maximum, followed by a plateau. The videos show that at the maximum force, the specimen developed a locally-narrow neck. The new material was then drawn into the neck as stretching continued. Necking and drawing is typical for many semicrystalline polymers.[55–57] The true stress *vs.* true strain behavior along the circumferential direction also showed strong strain hardening, but at higher strain than for axial stretching. Such anisotropy is likely attributable to the flow-alignment of polymer chains during extrusion, the process used to manufacture the tubes. Tensile tests at rates spanning two orders of magnitude showed similar behavior.[58]

3.2. Inflation tests

We first qualitatively describe a typical experiment in which the entire length of the tube is imaged (Fig. 4). To guarantee that a bulge would initiate within the field of view of the camera, we gently sanded a specific spot on the tube that was within the field of view. However, similar experiments without sanding provided identical results.[59]

Fig. 4(a) shows the pressure *vs.* volume curve during inflation. Here the x-axis is the volume increase ΔV (measured *via* the water height in transparent tube in Fig. 2) made non-dimensional by V_{o0}, which is the volume of the tube based on its undeformed outer diameter. At the inflation rate of 0.6 mL min^{-1} used in this experiment, the entire inflation processes up to bursting took approximately 300 s. Fig. 4(d) and (e) show the corresponding images taken from two cameras, one directly facing the sanded region, and the other mounted orthogonally. The volumes corresponding to these images are indicated by the vertical black dashed lines. The video corresponding to Fig. 4(d) is also available as SI. Fig. 4(b) shows the circumferential expansion estimated from the change in diameter far away from the bulge. Further, particle tracking analysis of the black markers allows quantifying the axial stretch far from the bulged region (Fig. 4(c)).

Four distinct stages can be identified in Fig. 4, as separated by the vertical black dashed lines. Between the initial undeformed state and point 1, pressure increases monotonically with only a slight change in diameter, and axial elongation of only 1%. From point 1 to 2, the pressure reduces gradually, and a slight local bulge becomes evident. During this gradual pressure decrease, the tube length reduces, and by point 2, the tube is shorter than its original length. We may compare the circumferential expansion far from the bulge with that expected from volume conservation assuming that the tube walls are incompressible:

$$\lambda_{\theta o}{}^2\lambda_z = \left(1 + \frac{\Delta V}{V_{o0}}\right) \quad (1)$$

where $\lambda_{\theta o}$ is the circumferential stretch of the outer surface of the tube, λ_z is the axial stretch, ΔV is volume increase, and V_{o0} is the volume of the tube based on its undeformed outer

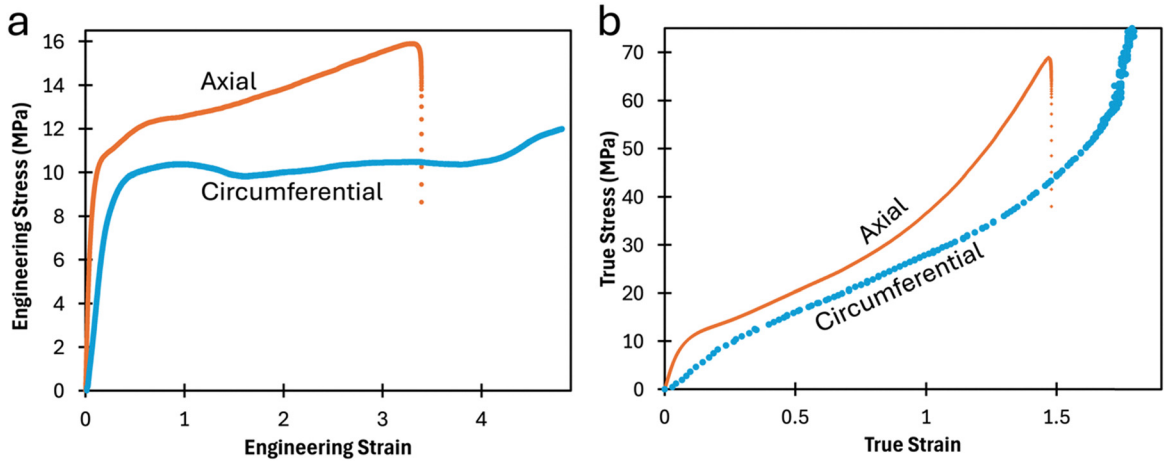

Fig. 3 (a) Engineering stress *vs.* engineering strain curves for an axially-stretched sample in orange and a circumferentially-stretched sample in blue. (b) Same data as a, but plotted with true values of stress and strain. The circumferential data at small strains are unreliable because the samples do not start from a stress-free state, see text and Section S2.

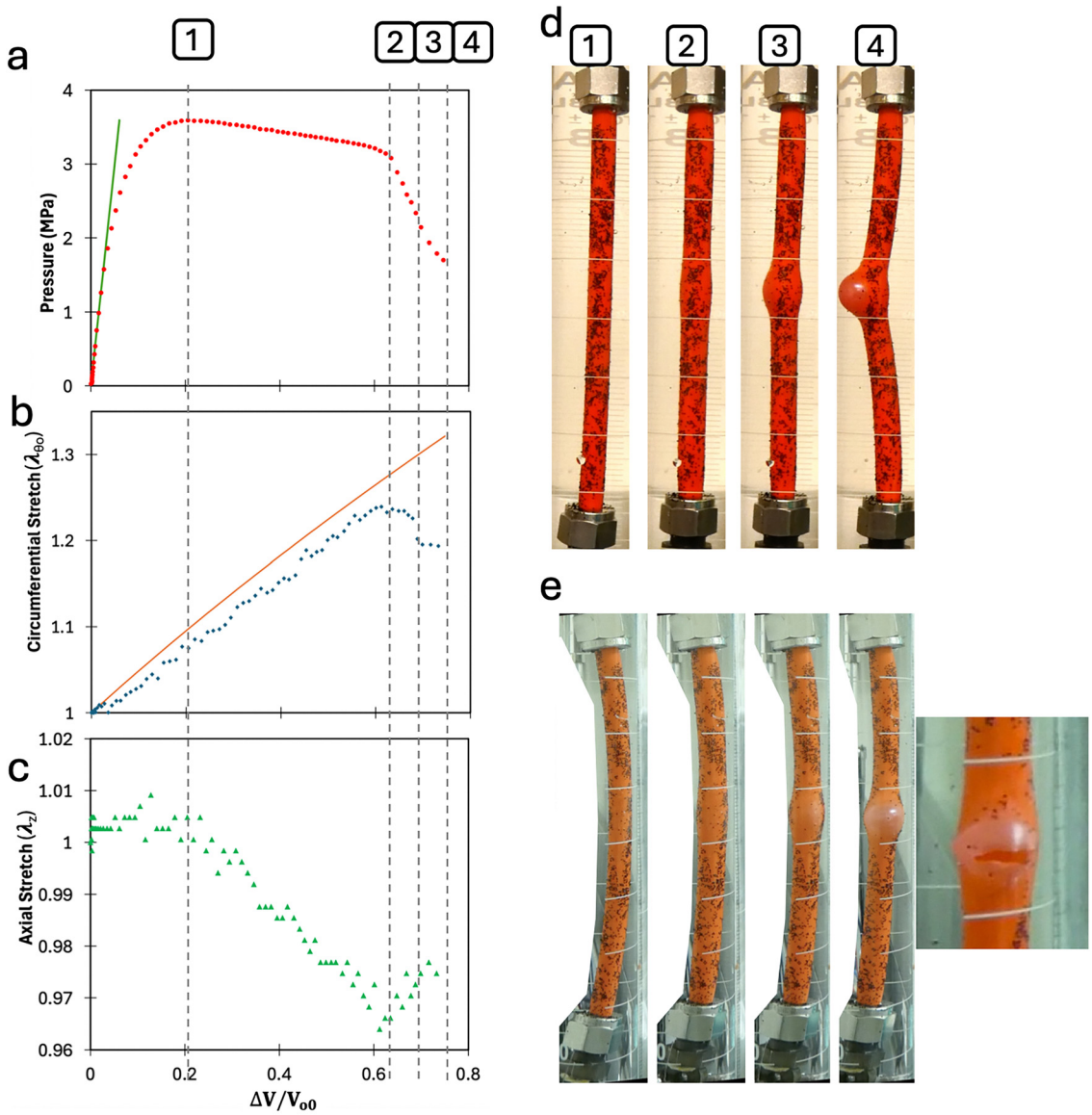

Fig. 4 Inflation experiment at 0.6 mL min^{-1} inflation rate. (a) Evolution of pressure with non-dimensional volume change. These are the same as the red points in Fig. 1(b). Straight line in a is fit to eqn (3) with circumferential modulus of 160 MPa as a fitting parameter. (b) Evolution of circumferential stretch. Line is the prediction of eqn (2) with no fitting parameters. (c) Evolution of axial stretch. (d) Images of the tube at the volumes corresponding to the four vertical dashed lines in a–c. (e) Images of the tube at the exact same volumes as in d, but taken from an orthogonal direction, see text for details. Rightmost image in e is after bursting; note the circumferentially-oriented crack.

diameter. Since the axial elongation is small (Fig. 4(c)), we set λ_z to 1 to obtain

$$\lambda_{\theta o} = \sqrt{1 + \frac{\Delta V}{V_{o0}}} \qquad (2)$$

Eqn (2) corresponds to the solid line in Fig. 4(b), *i.e.* the unbulged section closely follows the expected expansion until the bulge starts growing non-axisymmetrically.

Beyond point 2 the bulge grows rapidly (in less than 10 s) in a non-axisymmetric fashion and takes on the form of a nearly hemispherical "bubble". This bulging is accompanied by a rapid drop in pressure and slight axial lengthening (Fig. 4(b)). In addition, due to the drop in pressure, the unbulged region slightly shrinks in diameter, Fig. 4(b). The images at point 4 were taken just prior to failure. Beyond this point, the tube bursts by a circumferentially-oriented crack as mentioned in the Introduction. Multiple experiments showed modest variation in the time corresponding to the steep pressure drop, and in the steepness of the decrease in pressure. In some experiments (*e.g.* Fig. 5 below), the pressure appears to level off for a brief period before bursting. These variations may be due to minor defects in the tube that trigger inflation instability. Experiments at inflation rates in the range of 0.2 to 20 mL min^{-1} show similar behavior,[58] *i.e.* in contrast to the polyurethane tubes of our previous research,[5] the inflation behavior is qualitatively insensitive to rate.

Before proceeding, we note that metal tubes typically fail with an axially-oriented crack (*e.g.* Fig. S1e). This may be readily rationalized based on the fact that at small deformations, the hoop stress is larger than the axial stress (in fact, twice as large for a thin-walled tube). Polymeric tubes however show more variability, and Fig. S1a–d shows examples of cracks that may be axially- or circumferentially-oriented. We are unaware of literature explaining the reasons for these differences and will not discuss fracture further in this paper.

The pressure–volume curve at the early stages of inflation can be compared with that expected from linear elasticity. Since the axial strain is negligible, plane strain conditions are approximated. Thus, the following equation relates the pressure, P, to the increase in volume, ΔV, for an incompressible linearly-elastic thick-walled tube[60]

$$P = \frac{\Delta V}{V_{o0}} \frac{E}{3} \left(\frac{{R_{o0}}^2}{{R_{i0}}^2} - 1 \right) \quad (3)$$

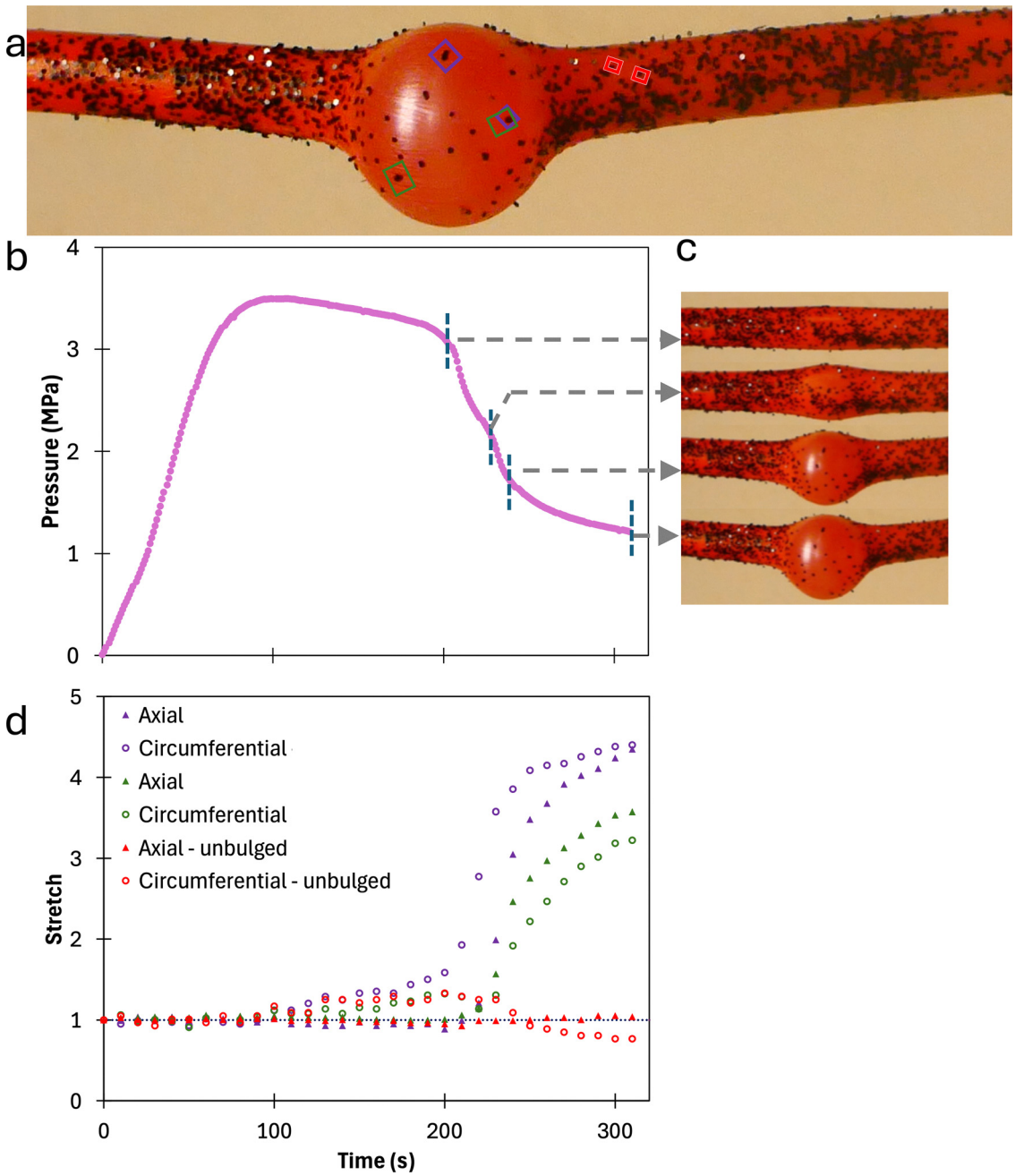

Fig. 5 (a) Image of the tube showing three pairs of markers used for quantifying the axial and circumferential stretches. Purple and green squares are used to quantify the bulged region, whereas red squares to quantify the unbulged region. (b) Pressure *vs.* time data during inflation. (c) Magnified view of the bulge at the time corresponding to the vertical dashed blue lines in (b). (d) Axial and circumferential stretches obtained from the pairs of markers on the bulge and unbulged region. Marker colors correspond to the colors of the squares in a. Note that images in a and c have been tilted for convenience even though the tubes were vertical during the experiment.

where R_{i0} and R_{o0} are the undeformed inner and outer radius, E is the elastic modulus, ΔV is volume increase, and V_{o0} is the volume of the tube based on its undeformed outer diameter. Using the modulus of 160 MPa from Section 3.1, eqn (3) is in good agreement with the data (green line of Fig. 4(a)). Thus, although the tubes have significant anisotropy at large strain, the small-strain modulus is approximately equal in the axial and circumferential directions.

The experiment of Fig. 4, which shows the behavior of the entire tube length, lacks the resolution to quantify deformation of the bulge itself. For strain quantification, further experiments were conducted at higher magnification with the camera mounted normal to the sanded region. For ease of visualization, this experiment was not conducted in the water-container. Fig. 5 shows that we can capture the bulge, and a portion of the tube outside the bulge, at a resolution of roughly 0.2 mm. Despite the higher resolution, it is not possible to precisely quantify the entire strain field since we only have 2D images from a single direction of this complex 3D deformation. Nevertheless, stretches can be estimated approximately by selecting pairs of markers (indicated by the small green, purple, and red colored squares in the image), and comparing their displacements. These markers are selected to be close to the surface directly facing the camera to reduce the effect of tube curvature. Fig. 5(d) shows the circumferential and axial stretches from three pairs of markers: two pairs selected to be in the bulged region (purple and green), and one pair selected to be in the non-bulged region (red).

During the initial rise in pressure when the deformations are small, the different locations have almost equal stretches confirming that the deformation is homogeneous. During the gradual decrease in pressure, the stretches corresponding to the purple and green pairs of markers (on the bulge) diverge from the red pair of makers (outside the bulge). However, for both the purple and green pairs, the circumferential stretches increase before the axial stretches, *i.e.* during the gradual pressure decrease, bulge growth is primarily circumferential. During the steep pressure drop however, the axial stretch in the bulge region increases sharply and eventually becomes comparable to the circumferential stretch. This is consistent with the hemispherical appearance of the bulge. Moreover, the fact that the two stretches are comparable may explain why the eventual rupture is not necessarily oriented axially (as for example, the metal tube in Fig. S1e) but may be oriented circumferentially. Simultaneously, the stretches corresponding to the red pair of markers reduce, indicating that the tube outside the bulge shows elastic recoil as the pressure decreases. Finally note that the area expansion estimated from the product of the two stretches well exceeds 15, *i.e.* prior to bursting, the non-axisymmetric bulge reaches a high level of biaxial stretch.

3.3. Irreversible deformation

The bulged region clearly undergoes large permanent deformation; this is evident from the image after the tube bursts (rightmost image in Fig. 4(e)). The experiments in this section address the question: at what point during inflation does irreversible deformation become important? Does it only become important after the bulge starts growing, or much earlier? Should the maximum in pressure be associated with irreversible deformation? In fact, Section 4 shows that as per the Tresca yield criterion, the tube wall is expected to yield at a pressure of 2.22 MPa – a value that is well below the maximum pressure during inflation. A more careful estimate (Section S4) suggests that the inner wall should yield at an even lower pressure of 1.71 MPa. Thus, yielding and irreversible deformation are expected even before the pressure maximum is reached. Accordingly, this section aims to quantify the onset of irreversible deformation.

One simple way to judge yielding and irreversible deformation of any system is to compare the shape before and after loading. In our case, if the tube had been straight, irreversible deformation prior to the pressure maximum would have been difficult to identify since, as per Fig. 4(b) and (c), dimensional changes up to the pressure maximum are small. Fortuitously however, the tubes have an intrinsic curvature, and therefore even a small degree of permanent strain gives a relatively large macroscopic shape change, which can be measured readily. Accordingly, five tubes were subjected to increasing degrees of inflation before unloading. Two inflations were stopped before the pressure maximum, one near the pressure maximum, and two past the pressure maximum into the region where pressure gradually reduced. The pressure–volume curves during all these tests are shown in Fig. 6(a).

Fig. 6(b) superposes the initial shape of each tube specimen before inflation in red and the final shape after the inflation-deflation in grey. The degree of straightening is seen to increase as the tubes are inflated to a greater extent. These before-and-after images were quantified by fitting the inner radius of the curved shape to the arc of a circle. The corresponding decrease in curvature is plotted in Fig. 6(c). The central conclusion is that a small decrease in curvature appears when deflated after a pressure of 2.5 MPa, which is in reasonable agreement with the value of 2.22 MPa expected for yielding (see Discussion and eqn (10) below). The changes in curvature increase steadily (*i.e.* tubes straighten more) with increasing levels of inflation, but there is no abrupt increase at the pressure maximum, *i.e.* the pressure maximum should not be ascribed to the initiation of yielding.

4. Discussion

We discuss three noteworthy aspects of inflation behavior: the maximum in pressure, the non-axisymmetric growth of the bulge, and the eventual growth into a hemispherical bubble before rupture.

First consider the pressure–volume behavior. The initial increase in pressure during inflation is readily captured by linear elastic theory, eqn (3). The behavior beyond the yield point depends on strain hardening behavior of the tube walls. If there is no strain hardening, the wall stress saturates at a constant value that is independent of inflation. If the degree of inflation is sufficiently small that the tube dimensions are nearly equal to undeformed dimensions, a constant wall stress

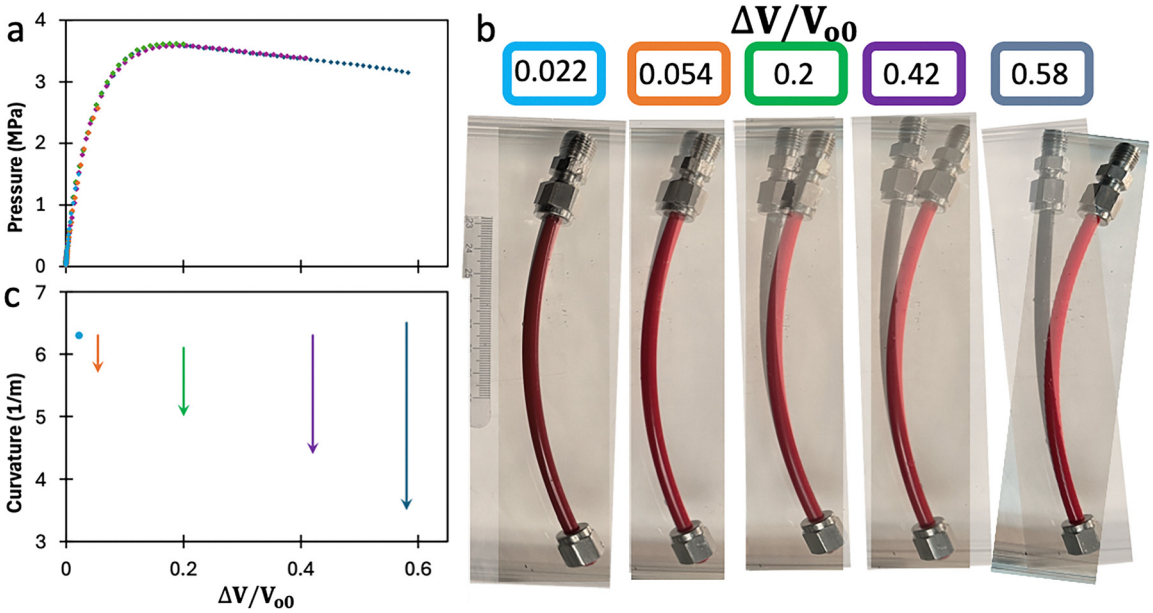

Fig. 6 (a) Pressure–volume curves for five tube specimens inflated to various pressures. (b) Each image shows an overlay of the initial shape of the tube before inflation in red and after deflation in gray. (c) Initial and final curvature after deflation, measured along the inner perimeter, for each sample. Each arrow is drawn to start at the initial curvature and end at the final curvature after deflating the tube.

immediately implies that the pressure must reach a plateau. If the tube walls show post-yield strain hardening, the wall stress increases gradually even beyond the yield point and hence the pressure is expected to increase gradually with inflation. Neither of these cases can predict a maximum in pressure. A pressure maximum can only arise if changes in tube dimensions (increase in diameter and decrease in wall thickness) are accounted for.

Consider an approximate plane strain thin-shell model to capture the physics from the previous paragraph. The tube is treated as a thin shell of mean radius $R_m = (R_o + R_i)/2$ and thickness $h = R_o - R_i$ in the inflated state. The undeformed radius and thickness respectively are $R_{m0} = (R_{o0} + R_{i0})/2$ and $h_0 = R_{o0} - R_{i0}$. For a tube that maintains cylindrical shape, a force balance (sometimes called Laplace equation) readily gives the expression

$$P = \frac{h}{R_m}\sigma_H \tag{4}$$

where $\sigma_H = \sigma_{\theta m}$ is the hoop stress in the shell walls. If the deformation is small, $h/R_m = h_0/R_{m0}$ is constant, and therefore it is immediately obvious that the pressure simply follows the hoop stress, and hence can only increase monotonically or reach a plateau, with inflation. To account for changes in tube dimensions, we assume that the walls are incompressible,

$$2\pi R_{m0} h_0 = 2\pi R_m h \tag{5}$$

Accordingly,

$$P = \frac{h_0}{R_{m0}}\frac{{R_{m0}}^2}{{R_m}^2}\sigma_H = \frac{h_0}{R_{m0}}\frac{1}{{\lambda_{\theta m}}^2}\sigma_H \tag{6}$$

where $\lambda_{\theta m} = R_m/R_{m0}$ is the circumferential stretch based on the mean radius, h_0 and R_{m0} are undeformed thickness and mean radius, and h and R_m are deformed thickness and mean radius respectively. Further the volume change can be related to the deformations by

$${\lambda_{\theta m}}^2\lambda_z = V_m/V_{m0} \tag{7}$$

where V_{m0} is the undeformed volume based on the mean radius and $V_m = V_{m0} + \Delta V$ is the deformed volume in the inflated state. Eqn (7) is similar to eqn (1), but now applied to a thin shell of radius R_m. Now assuming that the axial strain is small ($\lambda_z = 1$), as confirmed experimentally, eqn (6) can be rewritten in terms of volume changes

$$P = \frac{h_0}{R_{m0}}\frac{V_{m0}}{V_m}\sigma_H \tag{8}$$

All quantities with subscript 0 are fixed for a given sample. Thus, the pressure–volume behavior can show a maximum if the quantity σ_H/V_m has a maximum as V_m increases. Note that the dependence of σ_H on V_m depends on the constitutive behavior of the material. In contrast, the quantity V_{m0}/V_m is a purely geometric aspect, specifically that R_m increases due to inflation, which in turn reduces h due to wall incompressibility.

We now consider different scenarios for constitutive behavior of the walls. Taking the walls to be linearly elastic with the elastic modulus E, and under plane strain conditions

$$\sigma_H = \frac{E}{1-\nu^2}(\lambda_{\theta m} - 1) = \frac{4}{3}E\left(\sqrt{\frac{V_m}{V_{m0}}} - 1\right) \tag{9}$$

where $\nu = 0.5$ is the Poisson's ratio for the incompressible walls. Note that $(\lambda_{\theta m} - 1)$ is simply the circumferential strain. Combining eqn (8) and (9) gives an expression for pressure:

$$P = \frac{4}{3}\frac{h_0}{R_{m0}}\frac{V_{m0}}{V_m}E\left(\sqrt{\frac{V_m}{V_{m0}}} - 1\right) \tag{10}$$

Note that $V_m = V_{m0} + \Delta V$, and hence eqn (10) can be compared directly with the experimental data. Eqn (10) is shown as a solid blue line in Fig. 7 and on a larger scale in the inset to Fig. 7a. The functional form of the right-hand side implies a maximum pressure, which may be determined analytically at a V_m/V_{m0} value of 4, or $\Delta V/V_{m0}$ of 3. The location of the maximum is denoted by a vertical dashed line in the inset to Fig. 7a. Fig. S5 shows that, eqn (10) is in reasonable agreement with a more precise thin-shell analysis[2] that does not specify $\lambda_z = 1$, except that the more precise analysis predicts a pressure maximum at V_m/V_{m0} value of 3.27. Although approximate as compared to the precise analysis of Fig. S5, the benefit of eqn (10) is that the physical reason for the non-monotonic pressure evolution is transparent: the quantity inside the brackets grows with inflation because the hoop stress in eqn (4) grows, but the quantity outside the brackets reduces with inflation for the purely geometric reasons mentioned above.

This simple model can capture the existence of the maximum pressure as a coupling between geometric effects and constitutive behavior of the walls. However, the predicted volume at the maximum ($\Delta V/V_{m0} = 3$) far exceeds that observed experimentally. The likely reason is yielding: beyond the yield point, eqn (9) overestimates the increase in hoop stress with inflation, and hence the pressure from eqn (10) rises far higher than if we accounted for yielding.

We may expect yielding to occur when the hoop stress equals the yield stress (incidentally, this is equivalent to applying the Tresca yielding criterion to a thin-walled tube, because the shear stress is simply equal to half of the hoop stress). Taking the yield stress as 6.5 MPa, eqn (9) then predicts $V_m/V_{m0} = 1.083$, *i.e.* $\Delta V_m/V_{m0} = 0.083$, at the yield point, from which eqn (10) predicts a pressure of 2.22 MPa. This is in reasonable agreement with both: the pressure at which the tube starts straightening significantly, and also the pressure at which the measured PV curve deviates from linearity (Fig. 4). Beyond this pressure, one should expect significant deviations from eqn (10).

To capture post-yield behavior, we adopt the following constitutive behavior:

$$\left.\begin{aligned} \sigma_H &= \frac{E}{1-\nu^2}(\lambda_{\theta m} - 1) \quad \text{for } \sigma_H \le \sigma_y \\ \sigma_H &= \sigma_y + E_T(\lambda_{\theta m} - \lambda_y) \quad \text{for } \sigma_H > \sigma_y \end{aligned}\right\} \tag{11}$$

Here the first part of the equation is identical to eqn (9), and $\lambda_y = 1 + 3\sigma_y/4E$ is the stretch at the yield point, *i.e.* when $\sigma_H = \sigma_y$. in eqn (9). E_T represents the tangent modulus of the uniaxial stress–strain curve beyond the yield point. E_T is positive, but taken to be much less than E, thus causing the hoop stress to increase more mildly with inflation than expected from the linearly elastic behavior, eqn (9). Adopting eqn (11) as the constitutive behavior, the pressure is expected to follow eqn (10) up to the yield point, but beyond the yield point, combining eqn (11) and eqn (9)

$$P = \frac{h_0}{R_{m0}}\frac{V_{m0}}{V_m}\left[\sigma_y + E_T\left(\sqrt{\frac{V_m}{V_{m0}}} - \frac{3\sigma_y}{4E} - 1\right)\right] \quad \text{for } \sigma_H > \sigma_y \tag{12}$$

Consider first $E_T = 0$, *i.e.* no strain hardening. In this case, beyond the yield point, the hoop stress remains at σ_y, and eqn (12) predicts a monotonic decrease in pressure as the tube is inflated. This behavior is shown by the dashed green line in Fig. 7, and Fig. S7 shows that this is in excellent agreement with a more precise analysis of fully yielded tubes. Accordingly, there is a sharp pressure maximum at $P = 2.22$ MPa corresponding to the switch from eqn (10) to eqn (12) which occurs at the yield point.

With increasing strain hardening, eqn (12) predicts a pressure maximum beyond the yield point, *i.e.* the tube yields, followed by a further increase in pressure up to some maximum value. This latter behavior is consistent with our results which show that yield and irreversible deformation precedes the pressure maximum (Fig. 6). Not surprisingly, increasing the strain hardening coefficient increases the volume and pressure

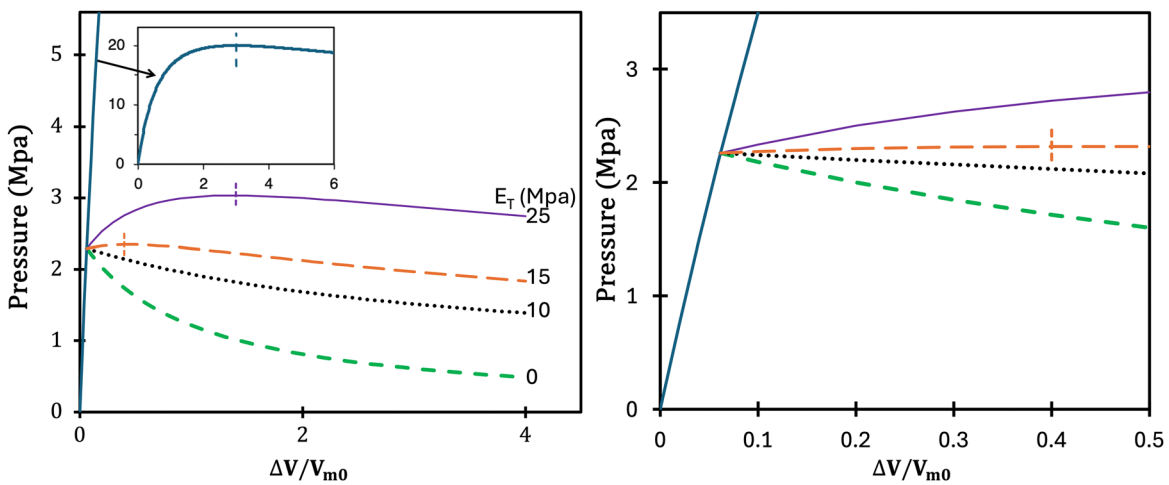

Fig. 7 Pressure–volume behavior predicted by the approximate thin shell model for various levels of tangential modulus parameter E_T. Right graph magnifies the behavior at small volume. Blue line is linearly elastic, eqn (10), which is shown over a larger range of pressures in the inset to the left graph. Small vertical lines indicate location of the maximum.

at the maximum. Incidentally, an E_T value of 20 to 30 MPa can reasonably fit the tensile experimental data immediately after the yield point, *i.e.* the values used for illustration in Fig. 7 are comparable to experiments. For such values, the shape of the pressure–volume curve also agrees with experiments.

The above analysis was conducted using a thin-wall assumption. The Section S2 shows that treating the tube as thick-walled changes the discussion slightly. Briefly, if the tube is treated as thick-walled[63] (1) PV behavior remains close to eqn (10) in the linear regime, (2) the first instance of yielding occurs at the inner wall at a pressure of 1.71 MPa, lower than the 2.22 MPa estimated above for a thin-walled model, and (3) the yield process is more gradual since yielding starts at the inner wall and propagates outwards. During this gradual yielding, the pressure increases even if $E_T = 0$; only once the yield surface reaches the outer wall does the pressure start reducing.

As mentioned in Section 3.1, this Discussion adopted 6.5 MPa as the yield stress. Yet, this value was assigned based on the stress at which the measured tensile stress–strain curve deviated from linearity. Using somewhat different criteria, a yield stress value as high as 8 MPa may be justified. In that case, all the above pressure estimates would increase proportionately. That would bring the maximum pressures in Fig. 7 in closer agreement with the experimentally-observed maximum. For example, if the yield stress were taken to be 8 MPa, the pressure at the yield point in Fig. 7 would be 2.73 MPa.

The presence of a pressure maximum only indicates that the homogeneous inflation (*i.e.* maintaining cylindrical shape) is unstable, thus making the tube susceptible to a bulge instability. Crucially (and different from a linearly elastic tube), any bulge that initiates is highly susceptible to localization. This is because any small imperfection induces strong local softening beyond the yield point. Since the hoop stress is the largest principal stress, the bulge, even if it starts axisymmetrically, has a strong driving force to become non-axisymmetric. Indeed, a computational study to be published,[61] but also available in a thesis,[58] shows the bulge becomes non-axisymmetric if E_T is small but remains axisymmetric if E_T is large.

While the presence of a yield stress can explain the non-axisymmetric deformation, it cannot explain the evolution of the bulge into a hemispherical bubble. Such behavior is not encountered in metal tubes; instead, the yield localizes strongly and proceeds to failure.[36,44] Polyvinyl chloride can show modest non-axisymmetric bulging, but not to the extent of forming a hemispherical bubble; instead, Fig. S1c shows that an axially-oriented neck appears which then thins locally prior to rupture. The hemispherical bulge growth seen in our experiments must therefore be attributable to the strain hardening that is evident at high strains in the tensile tests. Specifically, the strain hardening can limit, or at least reduce, local stretching (and hence reduce local thinning) by recruiting surrounding material into the bulge. Simulations[58,61] show that with strain hardening, the bulge can spread circumferentially and/or axially. However, if the strain hardening is weak, the bulge may rupture even before it starts spreading. Thus, tentatively we speculate that the tubes such as Fig. S1a–d have weak strain hardening and hence the non-axisymmetric bulge localizes without much spreading, causing rupture. In contrast, the polyethylene tubes examined here have stronger strain hardening, allowing the bulge to spread significantly before rupture. Note that the mechanical properties of the tubes in Fig. S1 were not reported, and hence this speculation cannot be evaluated at present.

5. An additional experiment: non-axisymmetric bulge propagation

The last paragraph of the previous section raises the question: what would happen if the strain hardening was much stronger? The behavior of hyperelastic tubes provides some guidance.[1,2,17,18] Neo–Hookean tubes show an axisymmetric bulge after some degree of inflation, and the bulge remains localized and grows circumferentially with continued expansion. However, if the constitutive behavior includes strain hardening, the local circumferential expansion saturates. With continued inflation, the bulge then propagates axially, which matches experimental observations on rubber tubes (Fig. 1(a), left image). Analogously, we speculate that even in tubes with yielding behavior, sufficiently strong strain hardening may limit the local bulge growth and force axial bulge propagation. This speculation is difficult to test directly because there is no means of tuning the strain hardening behavior of the material at will. Nevertheless, we may approximate strong strain hardening by inflating the tubes within a rigid external "limiter" of a larger diameter. Thus, as the bulge contacts the limiter, we anticipate that further local expansion of the bulge will be prevented, roughly analogous to the effect of strain hardening.

Experiments were conducted using as a limiter a transparent tube made of polyvinyl chloride which showed negligible deformation under experimental conditions and hence may be regarded as rigid. The inner diameter of the limiter tube was 11.4 mm, chosen to be smaller than the diameter at which the non-axisymmetric bulge would burst.

Fig. 8(a) shows the pressure *vs.* time curve during inflation at 0.6 mL min^{-1}, the same conditions as Fig. 4. Fig. 8(b) shows images of the experiment, and the corresponding video is available as SI. The initial bulge forms similar to that in the previous figures in this paper, and as in Fig. 4(a), the pressure decreases sharply as the bulge initiates. However, once the bulge contacts the limiter, the pressure increases slightly and reaches a plateau. During the plateau, the video and the images in Fig. 8(b) show stable axial propagation of the bulge. By equating the volumetric rate of inflation to the volume associated with bulge propagation, the bulge propagation speed, v, is expected to be

$$v = \frac{\text{Flow rate}}{\pi(R_l^2 - R_{o0}^2)} \tag{13}$$

where R_l is the limiter radius and R_{o0} is the undeformed outer radius of the tube. The propagation speed measured from the video is in excellent agreement with this expectation (not shown here but verified in Pazin[59] for multiple flow rates).

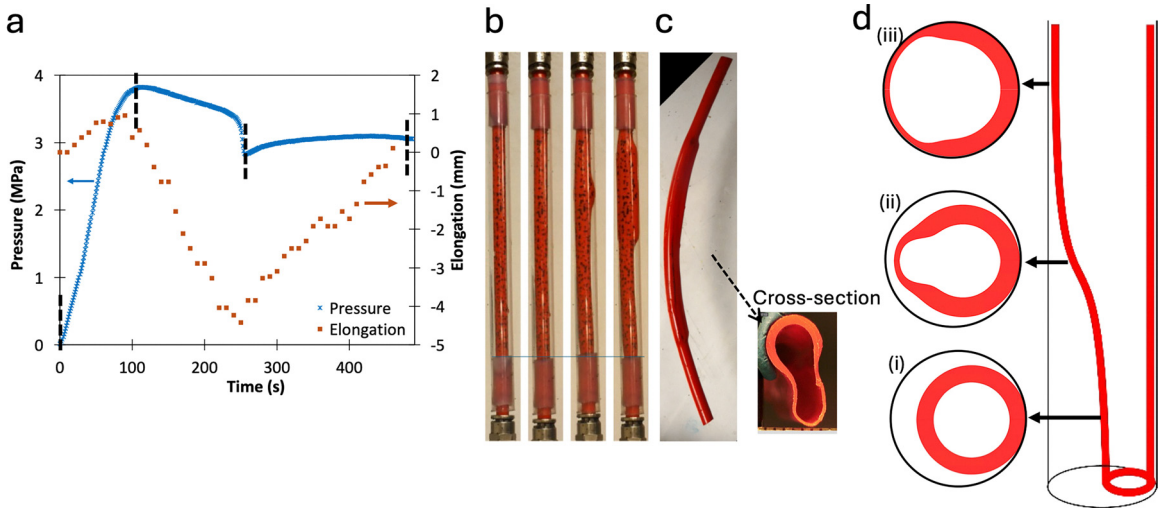

Fig. 8 (a) Pressure and length change *vs.* time curves of the inflated tube surrounding by a stiff limiter. (b) Images at the time-points corresponding to the dashed vertical lines in (a). (c) Tube after pressure is released showing a prominent ridge along the length of the tube. The cross-sectional view of the tube. (d) Schematics of cross sections ahead, at, and behind the bulge as the bulge propagates stably.

By tracking the bottom end of the tube, changes in tube length can be monitored. Fig. 8(a) shows that the bottom end first displaces downwards (tube length increases) and then upwards (tube length decreases) as the bulge initiates, and finally downwards again as the bulge propagates stably. The ratio of the end displacement to the tube length gives the mean axial stretch over the entire tube. Up to bulge initiation, this quantity is in good agreement with that shown in Fig. 4(c). But once the bulge starts propagating stably, deformation is entirely localized in the narrow zone within which the bulge propagates – as with other propagating instabilities, regions far ahead or far behind the propagation zone do not undergo any change. The change in tube length during propagation is relatively small; for example, in the time from 300 s to 420 s, the video shows the bulge propagating approximately 32 mm whereas the end-displacement is 2.5 mm, corresponding to a strain of 1.9%. Thus, unlike bulge propagation of a rubber hose,[1,2] the non-axisymmetric bulge propagation of Fig. 4 occurs with very little axial strain.

Upon releasing the pressure, the tube was found to be deformed permanently where a tall ridge appeared along the length of the tube. An image of the cross section (inset to Fig. 8(c)) shows a C-shaped portion whose thickness is close to that of the undeformed tube, and a much thinner portion that is bowed outwards. This latter section forms the ridge. Increasing the limiter radius reduces the plateau pressure at which the bulge propagates, increases the height of the ridge, and reduces the thickness of the wall comprising the ridge as shown in Fig. S7.[59] A limiter radius exceeding 12 mm did not allow stable propagation; instead, before or soon after the bulge touched the limiter, the tube ruptured. Crucially, for all limiters that allow bulge propagation, the ridged section itself has a uniform thickness throughout, which is characteristic of stable neck propagation.[55,56]

These observations suggest the schematic of Fig. 8(d) regarding the mechanics of stable propagation of the non-axisymmetric bulge. It shows a cartoon of the strain state at three cross sections that coexist along the length of the tube. The lowest cartoon labeled (i) shows a cross section far ahead of the bulge propagation zone. This region has already experienced peak pressure before the bulge first initiated and hence may have already undergone a modest degree of yielding as per the discussion of Section 3.3, nevertheless, its dimensions are very close to those of the undeformed tube. The middle cartoon labeled (ii) illustrates a section within the bulge propagation zone. Here the tube wall has a localized neck, which is propagating circumferentially. Such circumferential propagation can continue until the external diameter reaches the limiter diameter. The topmost cartoon labeled (iii) shows a cross section which is far behind the propagation zone where deformation is already complete. Here the outer surface of the tube is fully in contact with the limiter tube and hence further circumferential expansion is not possible. The cross section comprises two distinct thicknesses: a thin necked region which has undergone severe permanent deformation, and a thick unnecked region that has undergone only modest deformation. Upon releasing the pressure, the unnecked region recoils elastically, forcing the thin necked region to bow outwards and form a ridge.

To our knowledge, this is the first report of this type of non-axisymmetric bulge propagation, and it adds to the known examples of propagating instabilities such as bulge propagation in an inflated rubber tube; the buckle collapse of an externally-pressurized tube; neck propagation in a bar under tension.[1,56,62] Similar to the latter two instabilities, yielding is essential to this non-axisymmetric propagation instability.

We note one caveat. This section was motivated by the question of what happens to a non-axisymmetric bulge if the material is extremely strain hardening. Yet, the tests conducted here are not true strain hardening. The limiter only limits the overall increase in diameter, whereas true strain hardening would impose a limitation on the local strain everywhere.

6. Summary and conclusions

In summary, we have conducted an experimental study of the bulge instability in polyethylene tubes undergoing inflation. During inflation at a fixed rate, the pressure first increases, then reduces gradually, and then reduces steeply but in a continuous fashion. Quantitative video analysis shows that an axisymmetric bulge grows gradually starting from the pressure maximum. Later during inflation, the bulge starts growing non-axisymmetrically, eventually adopting the shape of a hemispherical bubble. It is this non-axisymmetric growth that causes a rapid drop in pressure and eventually rupture. These behaviors are very different from those of rubber tubes that are well-studied in the literature, polyurethane tubes from our own previous research, and metal tubes. We interpret the results relying on an approximate plane strain model which makes transparent the reasons why the pressure maximum appears. In general, the pressure evolution during tube inflation is a coupling of two factors: geometric (the tube diameter increases and walls become thinner with increasing inflation) and constitutive behavior of the material (the tube wall yields). We show that accounting for both of these can readily explain the pressure evolution during inflation. Even linearly elastic tubes are predicted show a maximum in pressure during inflation, albeit at a relatively high inflation volume. Yielding reduces the volume at the maximum significantly; the maximum appears either at the yield point (if the strain hardening is weak) or at a higher value (if the strain hardening is stronger). The decrease in pressure occurs due to change in deformed dimensions, and later due to non-axisymmetric bulge growth. The eventual formation of a hemispherical bubble must be attributable to the strain hardening at large strain which is seen in tensile tests. Finally, we show that if the bulge expansion is constrained by a rigid tube, the non-axisymmetric bulge can propagate in the axial direction. Upon depressurization, the tube is left with a prominent ridge that results from plastic deformation during bulge propagation. This appears to be a new kind of propagating instability which is only possible with materials that are both yielding and strain hardening.

Conflicts of interest

There are no conflicts to declare.

Data availability

Data and images published in this paper can be made available upon request to the corresponding author.

Supplementary information (SI) is available. This includes experimental videos and additional discussion and figures. See DOI: **https://doi.org/10.1039/d5sm00778j**.

Acknowledgements

This research was supported by NSF-DMR-2036164 and NSF-CMMI-1636064. We are grateful to Prof. Qihan Liu, University of Pittsburgh, for extensive discussions. This material is based upon work supported by (while serving at) the National Science Foundation. Any opinion, findings, and conclusions or recommendations expressed in this material are those of the author(s) and do not necessarily reflect the views of the National Science Foundation or of the Federal government.

References

1 S. Kyriakides and Y.-C. Chang, *Int. J. Solids Struct.*, 1991, **27**, 1085–1111.
2 S. Kyriakides and Y.-C. Chang, *Int. J. Solids Struct.*, 1990, **26**, 975–991.
3 H. Demirkoparan and J. Merodio, *Math. Mech. Solids*, 2020, **25**, 1459–1471.
4 J. Rodríguez and J. Merodio, *Mech. Res. Commun.*, 2011, **38**, 203–210.
5 F. Rouhani, J. W. Pazin, B. A. Young, Q. Liu and S. S. Velankar, *Soft Matter*, 2024, **20**, 4152–4164.
6 A. A. Alhayani, J. Rodríguez and J. Merodio, *Int. J. Eng. Sci.*, 2014, **85**, 74–89.
7 A. A. Alhayani, J. A. Giraldo, J. Rodríguez and J. Merodio, *Finite Elem. Anal. Des.*, 2013, **73**, 20–29.
8 M. Hejazi, Y. Hsiang and A. Srikantha Phani, *Proc. R. Soc. London, Ser. A*, 2021, **477**, 20200837.
9 T. Voňavková and L. Horný, *Comput. Methods Biomech. Biomed. Eng.*, 2020, **23**, 81–91.
10 L. Horný and M. Netušil, *Int. J. Mech. Sci.*, 2016, **106**, 95–106.
11 Y. B. Fu, S. P. Pearce and K. K. Liu, *Int. J. Non-Linear Mech.*, 2008, **43**, 697–706.
12 R. De Pascalis, W. J. Parnell, I. David Abrahams, T. Shearer, D. M. Daly and D. Grundy, *Proc. R. Soc. London, Ser. A*, 2018, **474**, 20180102.
13 Z. Petřivý and L. Horný, *Eur. J. Mech.*, 2022, **96**, 104763.
14 E. Benet, H. Zhu and F. J. Vernerey, *Phys. Rev. E*, 2019, **99**, 042502.
15 Z. Guo, J. Gattas, S. Wang, L. Li and F. Albermani, *Int. J. Mech. Sci.*, 2016, **115–116**, 665–675.
16 S. Wang, Z. Guo, L. Zhou, L. Li and Y. Fu, *J. Mech. Phys. Solids*, 2019, **124**, 536–554.
17 D. M. Haughton and R. W. Ogden, *J. Mech. Phys. Solids*, 1979, **27**, 489–512.
18 D. M. Haughton and R. W. Ogden, *J. Mech. Phys. Solids*, 1979, **27**, 179–212.
19 B. Lindgreen, V. Tvergaard and A. Needleman, *Modell. Simul. Mater. Sci. Eng.*, 2008, **16**, 085003.
20 B. Lindgreen, V. Tvergaard and A. Needleman, *Int. J. Solids Struct.*, 2008, **45**, 580–592.
21 M. J. Al-Chlaihawi, D. Desena-Galarza, H. Topol and J. Merodio, *Finite Elem. Anal. Des.*, 2025, **244**, 104309.
22 S. Moradalizadeh, H. Nazari, H. Topol and J. Merodio, *J. Appl. Comput. Mech.*, 2025, **11**, 1060–1074.
23 M. Takla, *Int. J. Mech. Sci.*, 2018, **141**, 303–315.
24 Y. Shi, P. D. Wu, D. J. Lloyd and J. D. Embury, *Eur. J. Mech. A/Solids*, 2010, **29**, 475–483.
25 S. Zha and H. Lan, *Int. J. Pressure Vessels Piping*, 2021, **189**, 104270.

26 Z. Abdelwahab, B. Abdelkader, H. Abderazek, B. Tayeb and M. Nouioua, 2024, preprint, DOI: 10.21203/rs.3.rs-2246408/v2.
27 X. Zheng, J. Wang and H. Chen, *J. Test. Eval.*, 2020, **48**, 4179–4189.
28 X. Zheng, X. Zhang, L. Ma, W. Wang and J. Yu, *Int. J. Pressure Vessels Piping*, 2019, **173**, 11–19.
29 Y. Tomita, A. Shindo and H. Kitagawa, *Int. J. Mech. Sci.*, 1981, **23**, 723–732.
30 C. Chu, *J. Appl. Mech.*, 1979, **46**, 889–894.
31 F. Majid and M. Elghorba, *Eng. Failure Anal.*, 2017, **71**, 157–165.
32 F. Majid, M. Safe and M. Elghorba, *Procedia Struct. Integr.*, 2017, **3**, 380–386.
33 F. Majid, A. Ouardi, M. Barakat and M. Elghorba, *Procedia Struct. Integr.*, 2017, **3**, 387–394.
34 F. Gugouch, M. Meknassi, M. Elghorba, A. Wahid, H. Mouradi, B. Hassan and A. Maziri, *Frat. Integrita Strutt.*, 2024, **18**, 192–204.
35 F. Gugouch, M. Elghorba, A. Wahid and B. Youssef, *Frat. Integrita Strutt.*, 2023, **17**, 218–228.
36 M. Larsson, A. Needleman, V. Tvergaard and B. Storakers, *J. Mech. Phys. Solids*, 1982, **30**, 121–154.
37 J. A. Jansen, Fractography of Plastic Pipe Failures, https://madisongroup.com/fractography-of-pipe-failures/, (accessed 15 April 2025).
38 S. Zha, H. Lan and H. Huang, *Int. J. Pressure Vessels Piping*, 2022, **198**, 104663.
39 H. Teodorescu Draghicescu, M. L. Scutaru and S. Vlase, *Materials*, 2023, **16**, 6944.
40 A. Kulkarni, P. Biswas, R. Narasimhan, A. A. Luo, R. K. Mishra, T. B. Stoughton and A. K. Sachdev, *Int. J. Mech. Sci.*, 2004, **46**, 1727–1746.
41 Y. P. Korkolis and S. Kyriakides, *Int. J. Plast.*, 2008, **24**, 509–543.
42 M. Sorine, C. H. M. Simha, I. Van Riemsdijk and M. J. Worswick, *Int. J. Mech. Sci.*, 2008, **50**, 1411–1422.
43 Y. P. Korkolis and S. Kyriakides, *Int. J. Plast.*, 2009, **25**, 2059–2080.
44 M. Sun and P. Bunch, in Proceeding of ETCE2002, 2002.
45 M. Takla, *Int. J. Press. Vessels Pip.*, 2018, **159**, 73–83.
46 M. Takla, *Mar. Struct.*, 2019, **64**, 246–262.
47 T. A. Brabin, T. Christopher and B. N. Rao, *Multidiscipline Modeling in Materials and Structures*, 2009, vol. 5, pp. 29–42.
48 E. J. Hearn, *Mechanics of materials 1: an introduction to the mechanics of elastic and plastic deformation of solids and structural materials*, Butterworth-Heinemann, 1997, pp. 198–251.
49 A. R. Ragab and S. Eldin Bayoumi, *Engineering Solid Mechanics: Fundamentals and Applications*, 1998.
50 H. Topol, H. Demirkoparan and T. J. Pence, *Eur. J. Mech. A/Solids*, 2019, **77**, 103800.
51 K. Y. Volokh, *J. Mech. Phys. Solids*, 2007, **55**, 2237–2264.
52 A. Goriely, *The Mathematics and Mechanics of Biological Growth*, Springer, New York, 2017.
53 H. Topol, H. Nazari, M. Stoffel, B. Markert, J. Lacalle and J. Merodio, *Thin Wall Struct.*, 2024, **197**, 111562.
54 H. Topol and T. J. Pence, *Mech. Soft Mater.*, 2024, **6**, 7.
55 R. G. Ramachandran, S. Hariharakrishnan, R. Fortunato, S. D. Abramowitch, S. Maiti and S. S. Velankar, *Soft Matter*, 2018, **14**, 4977–4986.
56 J. W. Hutchinson and K. W. Neale, *J. Mech. Phys. Solids*, 1983, **31**, 405426.
57 I. M. Ward, Mechanical properties of solid polymers, *Mechanical Behavior of Solid Polymers*, J. W. Arrowsmith Ltd, Bristol, 1971.
58 F. Rouhani, PhD Thesis, *In progress*, University of Pittsburgh, 2025.
59 J. W. Pazin, MS Thesis, University of Pittsburgh, 2024.
60 A. R. Ragab and S. Eldin Bayoumi, *Engineering Solid Mechanics: Fundamentals and Applications*, 1st edn, 1998, ch. 6, p. 246.
61 F. Rouhani and S. Velankar, unpublished work.
62 V. D. Do, P. Le Grognec and P. Rohart, *Eur. J. Mech. A/Solids*, 2023, **98**, 104861.
63 A. R. Ragab and S. Eldin Bayoumi, *Engineering Solid Mechanics: Fundamentals and Applications*, 1998, ch. 12, pp. 865–879.

